Land surface temperature from Ka band (37 GHz) passive microwave observations

T. R. H. Holmes,[1] R. A. M. De Jeu,[1] M. Owe,[2] and A. J. Dolman[1]

Received 11 April 2008; revised 21 November 2008; accepted 17 December 2008; published 25 February 2009.

[1] An alternative to thermal infrared satellite sensors for measuring land surface temperature (T_s) is presented. The 37 GHz vertical polarized brightness temperature is used to derive T_s because it is considered the most appropriate microwave frequency for temperature retrieval. This channel balances a reduced sensitivity to soil surface characteristics with a relatively high atmospheric transmissivity. It is shown that with a simple linear relationship, accurate values for T_s can be obtained from this frequency, with a theoretical bias of within 1 K for 70% of vegetated land areas of the globe. Barren, sparsely vegetated, and open shrublands cannot be accurately described with this single channel approach because variable surface conditions become important. The precision of the retrieved land surface temperature is expected to be better than 2.5 K for forests and 3.5 K for low vegetation. This method can be used to complement existing infrared derived temperature products, especially during clouded conditions. With several microwave radiometers currently in orbit, this method can be used to observe the diurnal temperature cycles with surprising accuracy.

Citation: Holmes, T. R. H., R. A. M. De Jeu, M. Owe, and A. J. Dolman (2009), Land surface temperature from Ka band (37 GHz) passive microwave observations, *J. Geophys. Res.*, *114*, D04113, doi:10.1029/2008JD010257.

1. Introduction

[2] Land Surface Temperature (T_s) is defined as the thermodynamic temperature of the uppermost layer of the Earth's surface. T_s is an important variable in the processes controlling the energy and water fluxes over the interface between the Earth's surface and the atmosphere. For continental- to global-scale modeling of these land surface processes there is need for long-term remote sensing–based T_s for validation and data assimilation procedures. Furthermore, T_s is a key input variable in numerous soil moisture retrieval methodologies from space observations [e.g., *Kerr et al.*, 2001; *Owe et al.*, 2001; *Njoku et al.*, 2003; *Verstraeten et al.*, 2006].

[3] Continental- to global-scale modeling requires T_s to be an area averaged value for each model grid square, typically sized between 0.5 and 2.0°. Remote sensing is ideally suited to give area averaged values at this spatial resolution. Commonly used global T_s products are derived from thermal infra red (TIR) sensors that are integrated in many satellite systems (e.g., polar orbiting AQUA, as well as geostationary platforms like GOES and METEOSAT). The spatial resolution of TIR measurements ranges from 1 to 5 km for polar orbiting satellites to 50 km for geostationary platforms. Assuming that the land surface emissivity is known, the actual temperature of the land surface can be derived from TIR measurements under clear skies. The TIR measurements usually need a correction for atmospheric constituents like water vapor, aerosols and particulate matter, and no observations are possible under clouded conditions. The latter is an important limitation because on average 50% of the land surface is covered by clouds [*Rossow et al.*, 1993].

[4] Passive microwave observations can be an alternative, or an addition to TIR sensors, for measuring T_s, in particular at the Ku band (18 GHz) or Ka band (37 GHz). Observations within these channels are typically divided in horizontal and vertical polarization. The vertical polarized channel is better suited for temperature sensing than the horizontal channel because it is less sensitive to changes in soil moisture at incidence angles of 50–55°. Of these two microwave bands, Ka band is the more appropriate frequency to retrieve T_s because it balances a reduced sensitivity to soil surface characteristics with a relatively high atmospheric transmissivity [*Colwell et al.*, 1983]. The sensitivity to soil surface parameters is lower at Ka band than at Ku band because vegetation scatters the surface emission more effectively. As a result, even a thin vegetation cover is opaque to $T_{B,37V}$ emission. The use of $T_{B,37V}$ for deriving T_s is limited by snow, frost, and frozen soil, as these conditions have a large effect on the emissivity that cannot easily be parameterized. The atmosphere appears more opaque at Ka band than at Ku band, resulting in an effect of the atmospheric temperature. Also, rain bearing clouds or active precipitation with droplets close to the size of the wavelength (8 mm for 37 GHz) will scatter the microwave emission [*Ulaby et al.*, 1986]. $T_{B,37V}$ observations have a spatial resolution of 10 to 25 km, which is somewhat higher than the resolution of current global land surface models, but lower than most TIR measurements.

[1]Department of Hydrology and Geo-Environmental Sciences, Vrije Universiteit, Amsterdam, Netherlands.
[2]Hydrological Sciences Branch, NASA Goddard Space Flight Center, Greenbelt, Maryland, USA.

Copyright 2009 by the American Geophysical Union.
0148-0227/09/2008JD010257

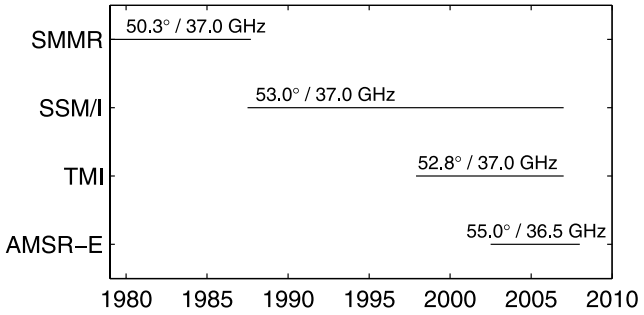

Figure 1. Operating years of microwave radiometers in orbit. The SSM/I sensor has been on several overlapping DMSP missions, and the AMSR-E sensor is included in the AQUA and WINDSAT missions.

[5] Besides these theoretical considerations, there is an important additional advantage to using either Ku band or Ka band and that is that these channels have been a constant part of satellite microwave missions since the late 1970s. Continuous measurements of $T_{B,37V}$ are now available from 1978 to the present from the Scanning Multichannel Microwave Radiometer (SMMR), the Special Sensor Microwave Imager (SSM/I), the TRMM Microwave Imager (TMI) and the Advanced Microwave Scanning Radiometer (AMSR-E), see Figure 1. These radiometers are all on polar orbiting satellites with global coverage, except the TMI that has an equator orbiting path between 40° north and south. In the future, the current missions will be continued and expanded (TRMM by the Global Precipitation Monitoring mission (GPM) Microwave Imager, AMSR-II on the GCOM-W, and a new Microwave Radiometer Imager (MWRI) is planned on the Chinese FY-3).

[6] At this point it is important to qualify how T_s is defined. The depth of the surface layer that T_s refers to depends on the sensor and the composition of the land surface in the sensor footprint. For bare surfaces, T_s represents the soil temperature at a shallow depth that depends on view angle, wavelength, and the surface characteristics (e.g., roughness, wetness, and soil texture). This thermal sampling depth is $\sim$50 μm for TIR frequencies, and at 37 GHz between 1 mm for a wet soil and up to 10 mm for a dry soil [*Ulaby et al.*, 1986]. When the surface is covered with vegetation, T_s represents the canopy surface temperature. In this paper, T_s refers to the area weighted average of the temperatures of the various land covers within a specific scene. As will be shown, at 37 GHz the vegetation is relatively opaque, and for most of the Earth (60%) T_s will effectively represent the vegetation canopy temperature.

[7] In the past, several authors used the 37 GHz signal to derive surface temperature for different well defined study sites and observed a strong linear relationship between $T_{B,37V}$ and T_s [e.g., *Owe et al.*, 2001; *Owe and Van de Griend*, 2001; *De Jeu and Owe*, 2003]. Other authors have tried multi-frequency approaches [e.g., *Fily et al.*, 2003], but these techniques have been more difficult to apply globally. This paper will continue with the single frequency approach and examine the potential of 37 GHz passive microwave observations for deriving land surface temperature at global scales. Simulation studies are used to test the theoretical influence of the most important rs that affect the relationship between the T_s and the measured $T_{B,37V}$ at the top of the atmosphere. On the basis of these simulations, a single linear relationship between T_s and $T_{B,37V}$ is derived, that can then be applied globally. Comparisons to field data are used to validate this approach.

2. Materials and Methods

2.1. Ground Measurements

[8] FLUXNET is a network of meteorological towers spanning the entire globe [*Baldocchi et al.*, 2001]. From this database 17 sites are selected that have good records of longwave radiation, sensible heat flux and air temperature for the year 2005, with a temporal resolution of a half hour. Secondary variables for this analysis are net radiation and wind speed. These sites represent a variety of vegetation types and climates (see Table 1). The dominant IGBP land cover class for the surrounding 0.15° grid box is based on the MOD12Q1 Land Cover Product [*Belward et al.*, 1999]. The reader is referred to http://www.fluxnet.ornl.gov for a detailed description of all sites.

[9] As discussed previously, T_s is the integrated temperature of all the land surface covers in a given radiometric footprint. It follows then that it cannot be measured at a single point, nor is it easily estimated by multiple observations of the soil and canopy surfaces. One way to address this problem is by comparing T_s with the emitted longwave radiation. The longwave flux is a direct function of the physical temperature of the land surface, and like T_s, is representative of all the radiating surfaces in the sensor's view. The benefit of this approach is that no temperature conversions need to be made to compare temperatures from different depths. Instead, the longwave emissivity (ε) must be determined for each site separately to calculate the land surface temperature, now denoted T_{LW}. The procedure to determine ε is outlined below.

[10] Although the use of the longwave flux makes it easier to compare the satellite derived temperature with ground measurements, the footprint of the flux tower measurement remains much smaller than that of the satellite. Heterogeneity within the satellite footprint can therefore cause a bias between the two measurements, if the location of the flux tower is not representative for the 25 $\times$ 25 km area. For this reason the satellite derived land surface temperature will principally be validated against the ground measurements in terms of correlation R^2 and standard error of estimate (SEE), and not in terms of bias.

2.2. Longwave Emissivity

[11] The relationship between outgoing longwave radiation ($F_{LW,up}$) and longwave surface temperature, denoted T_{LW}, is based on the Stefan-Boltzmann law, according to:

$$F_{LW,up} = \varepsilon \sigma T_{LW}^4 \tag{1}$$

where ε is the broadband emissivity for the entire TIR spectral region and σ is the Stefan-Boltzmann's constant ($\sigma = 5.6697 \times 10^{-8}$ Wm^{-2} K^{-4}).

[12] According to *Penman* [1948], the sensible heat flux (H) can be described as $H = C\Delta T$, with C representing vegetation-dependent parameters and boundary conditions. ΔT is the temperature difference between the land surface

Table 1. Geographical Location, IGBP Vegetation Class, and LW Emissivity for 17 Field Sites

ID	Site Name	Latitude	Longitude	Vegetation Class at Site	Vegetation Class 0.15°	Emissivity at Site
			Low-Vegetation Group			
A	Arizona,[a] US	31.59°N	110.51°W	grasslands	grasslands	0.946
B	Fort Peck Montana,[a] US	48.31°N	105.10°W	grasslands	cropland/natural vegetation mosaic	0.961
C	Brookings South Dakota,[a] US	44.35°N	96.84°W	croplands	croplands	0.971
D	Bondville Illinois,[a] US	40.01°N	88.29°W	croplands	croplands	0.961
E	Bondville comp. Illinois,[a] US	40.01°N	88.29°W	croplands	croplands	0.938
F	Cabauw,[b] NL	51.97°N	4.93°E	croplands	croplands	0.995
G	Gebesee,[c] DE	51.10°N	10.91°E	croplands	croplands	0.987
H	Mitra II,[d] Evora, PT	38.54°N	8.00°E	cropland/natural vegetation mosaic	cropland/natural vegetation mosaic	0.980
			High-Vegetation Group			
I	Ozark Missouri,[a] US	38.74°N	92.20°W	deciduous broadleaf forest	cropland/natural vegetation mosaic	0.970
J	Morgan Monroe Indiana, US	39.32°N	86.41°W	deciduous broadleaf forest	deciduous broadleaf forest	0.995
K	Collelongo beech,[c] IT	41.85°N	13.59°E	deciduous broadleaf forest	mixed forest	0.960
L	Mehrstedt1,[f] DE	51.28°N	10.65°E	mixed forest	croplands	0.989
M	Loobos,[g] NL	52.17°N	5.74°E	evergreen needleleaf forest	croplands	0.995
N	Le Brai,[h] FR	44.72°N	0.77°W	evergreen needleleaf forest	mixed forest	0.988
O	Black Hills South Dakota,[a] US	44.16°N	103.65°E	evergreen needleleaf forest	evergreen needleleaf forest	0.971
P	North Carolina, US	35.98°N	79.09°W	evergreen needleleaf forest	mixed forests	0.990
Q	Yatir,[i] IL	31.35°N	35.05°E	evergreen needleleaf forest	barren or sparsely vegetated	0.994

[a] *Hollinger et al.* [2005].
[b] *Beljaars and Bosveld* [1997].
[c] *Anthoni et al.* [2004].
[d] *David et al.* [2004].
[e] *DeAngelis et al.* [1996].
[f] *Scherer-Lorenzen et al.* [2007].
[g] *Dolman et al.* [2002].
[h] *Kowalski et al.* [2003].
[i] *Grunzweig et al.* [2003].

and the air. By this definition, $H = 0$ when $\Delta T = 0$. It follows that for a series of measurements the regression line of H against ΔT goes through zero. The ε can now be determined for each field site by optimizing the ΔT so that the regression (forced through zero) of H against ΔT has the lowest RMS error. This procedure (A) is applied for every month separately of the 2005 data and gives robust results when the ΔT explains a substantial part of the variance in H (we use a minimum R^2 of 0.5). The H values are considered reliable when the net radiation is more than 25 Wm^{-2} and the wind speed is more than 2 ms^{-1}. Figure 2a shows an example of the optimized ΔT from the cropland site C in Brookings, South Dakota, US, for August 2005. The points denoted by pluses are used for the optimization, the dots are the values that have either a low net radiation flux or a low wind speed.

[13] The above procedure A does not work when the variation in H cannot be explained by ΔT. This is the case when the roughness length of the vegetation is high, resulting in only a minimal difference between the vegetation and air temperature (T_a). For this situation it is assumed that $T_s = T_a$, and that the integrated temperature T_s is fully determined by the canopy temperature. The ε is now derived by minimizing the RMS error between T_s and T_a. Figure 2b shows an example of the resulting ΔT according to this procedure B, for the forest site P in North Carolina, US, for August 2005. Figure 2b illustrates that the variance in H cannot be explained by the temperature difference between the canopy and the air.

[14] The retrieved ε per month is indicated in Figure 3 for each site. The emissivity as determined following procedure A is indicated by a dot for $R^2 > 0.5$. For the months with a lower correlation, the value is rejected and the alternative procedure B is used where $T_s = T_a$. The emissivity according to this method is indicated by a circle. If more than 4 months have a high squared correlation, the average value for the whole year is based on procedure A, otherwise it is based on the alternative method. The resulting average ε for each site is listed in the graph and indicated by the horizontal line. It represents the effective longwave emissivity for the footprint of the flux measurements. Note that the emissivity can change during the year, especially if the surface is barren for part of the year (e.g., sites A and H).

[15] The values may be compared to MODIS emissivities for the wavelengths between 8 and 12 μm. *Snyder* [1999] lists them for the same IGBP classes: grasslands ($\varepsilon = 0.96$); croplands ($\varepsilon = 0.97–0.98$); deciduous broadleaf forest ($\varepsilon = 0.97$); and evergreen needle leaf forest ($\varepsilon = 0.99$). The emissivities are comparable, although the field values for cropland have a high variability. The high emissivity for the cropland of Cabauw (site F) can be explained by high percentage of water (with $\varepsilon = 0.99$). Black hills (site O) has a low emissivity compared to the rest of the forest sites and the MODIS emissivity, this is probably because of the open canopy.

[16] The year averages of ε are subsequently used to calculate T_{LW} for each site. For the comparison with the satellite observations, the ground measurement of T_{LW} is selected that is within 15 minutes of the satellite observation.

2.3. Satellite Observations

[17] Vertically polarized brightness temperatures in the Ka band are currently observed by various satellites (see Figure 1). In this study, we analyze the brightness temperature as observed by AMSR-E on board the Sun synchronous and polar orbiting AQUA satellite [*Ashcroft and Wentz*,

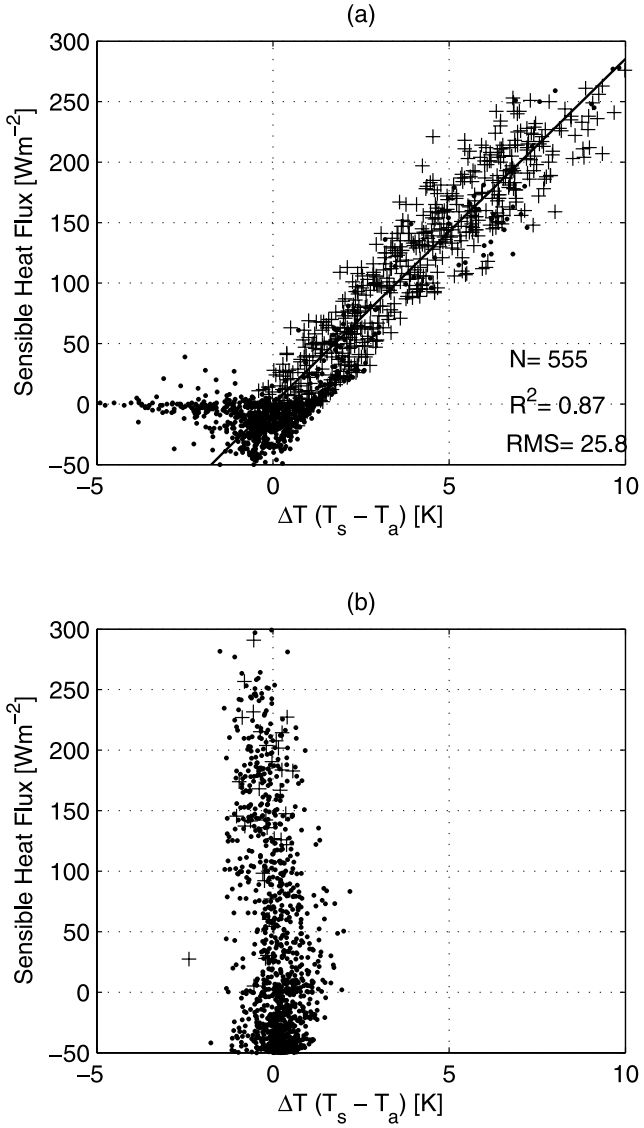

Figure 2. Sensible heat flux against optimized ΔT for (a) cropland site C and (b) forest site P. The cropland site is an example where procedure A works well because of a high R^2 between H and ΔT for points denoted by pluses. The forest site is an example with no correlation where procedure B has to be applied.

2003]. AMSR-E has a 36.5 GHz channel at 55° incidence angle. Equator overpass times are at 1330 LT for the ascending path and 0130 LT for the descending path. The revisit time at the equator is ~3 days. For each ground location of Table 1 we have extracted a time series of satellite brightness temperature observations for the year 2005 based on the Level 2A spatially resampled swath data. This time series includes the nearest points within either the ascending or the descending over passes.

[18] For two selected ground sites (North Carolina (P) and Montana (B), US) $T_{B,37V}$ is extracted for two additional satellites. The first one is the TMI on board the equator orbiting TRMM satellite [*Kummerow et al.*, 1998]. The overpass times of TRMM vary through the year. The second radiometer is the SSM/ oard the polar orbiting DMSP [*Armstrong et al.*, 1994]. Data are extracted from the fl3 platform with equator overpass times at 0600 and 1800 LT and a 4–5 day revisit time.

2.4. Radiative Transfer Model for Ka Band

[19] Brightness temperature as measured by satellite sensors can be simulated by radiative transfer models. A commonly used model that describes the microwave emission above a vegetated surface is the zero-order scattering model, sometimes called the omega-tau model [*Mo et al.*, 1982]. In this paper we use this omega-tau model to simulate the 37 GHz vertically polarized brightness temperature ($T_{B,37V}$) at the top of the atmosphere.

[20] The dielectric constant is modeled according to the mixing model by *Wang and Schmugge* [1980], which is adapted for high frequencies by *Calvet et al.* [1995]. The effect of roughness on the emissivity is corrected with the parameters Q for the cross polarization and h for the roughness height [*Wang and Choudhury*, 1981].

[21] The temperature of the soil surface is considered the same as the canopy temperature ($T_s = T_c$). Published values of single scattering albedo (ω) at this frequency are rare, especially for natural vegetation. *Pampaloni and Paloscia* [1986] found values of $\omega = 0.03$ to $\omega = 0.06$ for crops, while values averaging around $\omega = 0.1$ were found for savannah surfaces [*Van de Griend and Owe*, 1994].

[22] The atmospheric transmissivity is a function of the zenith atmospheric opacity (τ_a) and incidence angle ($\Gamma_a = e^{-\tau_a/\cos\theta}$). At 37 GHz, the atmospheric opacity varies between $\tau_a = 0.05$ and $\tau_a = 0.20$ depending on atmospheric water content [*Ulaby et al.*, 1986].

2.5. Simulation Experiments

[23] The radiative transfer model for $T_{B,37V}$ is used to test the sensitivity of the $T_{B,37V}/T_s$ relationship to the most important input parameters. For this purpose simulations were conducted that model the $T_{B,37V}$ for $T_s = 300$ K and for two scenarios; a typical vegetated surface and an extremely dry, bare surface (see Table 2). The purpose of these simulations is to calibrate the radiative transfer model and to determine the sensitivity to various input parameters.

[24] The vegetated scenario has medium volumetric soil water content (W_c) of 25%. The soil texture parameters are typical for a silt loam, with a porosity of 50% and a wilting point of 13%. The texture of a silt loam is chosen because the wilting point value is between the values for sand (3%) and clay (27%). At Ka band, even a thin vegetation cover becomes nontransmissive to the emission from the surface. Therefore, the transmissivity will in general be low and a default value of $\Gamma_v = 0.2$ is used. The atmosphere in this scenario is typical for a temperate climate, with 9 mm of precipitable water and no liquid water. This corresponds to a $\tau_a = 0.05$ (or $\Gamma_a = 0.9$ at an incidence angle of 55°).

[25] The dry, bare scenario has a low W_c of 10% and high vegetation transmissivity ($\Gamma_v = 0.9$). The soil texture parameters are typical for sand, with a porosity of 44% and a wilting point of 3%. Sand is chosen because the persistently dry surfaces do not accumulate clay particles. The atmosphere in this scenario is typical for a desert climate with 45 mm of precipitable water and no cloud liquid water content. This corresponds to a $\tau_a = 0.15$ (or $\Gamma_a = 0.74$ at an incidence angle of 55°).

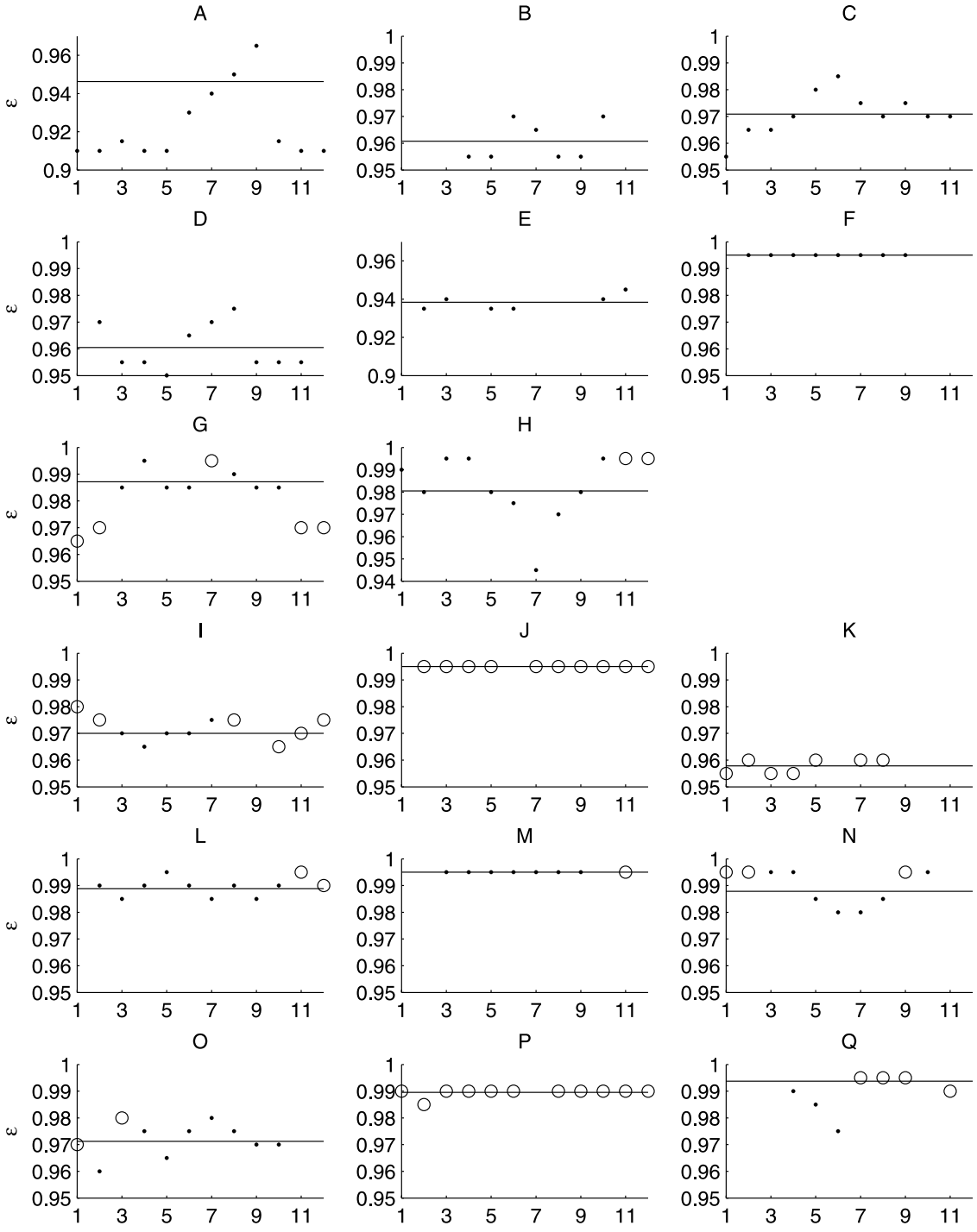

Figure 3. Monthly longwave emissivities for the ground sites. The letters above each plot refer to the site IDs in Table 1. The average value for the whole year is indicated by the horizontal line, and markers indicate retrieval procedure: procedure A (dot) and procedure B (circle).

Table 2. Input Parameters for the Simulation Experiments[a]

	Vegetated Surface	Dry, Bare Surface
Water content (%)	25	5
Soil type	Silt loam	Sand
Vegetation transmissivity (−)	0.2	0.9
Atmospheric transmissivity (−)	0.9	0.74
Roughness (−)	0.2 (0.035)	0.2 (0.035)
Cross polarization (−)	0.2 (0.039)	0.2 (0.039)
Single scattering albedo (−)	0.06 (0.01)	0.06 (0.01)

[a]In parentheses is the standard deviation attributed to the parameter.

[26] The surface roughness, cross polarization, and single scattering albedo are somewhat difficult to quantify, so they are used to calibrate the radiative transfer model to approximate the derived general relation in both scenarios. Furthermore, we describe the effective air temperature as a function of the surface temperature [*Bevis et al.*, 1992]: $T_e = 70.2 + 0.72T_s$ (all units in Kelvin).

[27] The influence of each of the input parameters on the simulated $T_{B,37V}$ is tested by varying them over a realistic range, while holding the other parameters constant. Variations from the calibrated default scenario will indicate sensitivity. Secondly, the sensitivity of the model to spatial variations in soil moisture and vegetation density is tested with observed global maps of these input variables.

3. Results

3.1. General Solution

[28] The aim of this paper is to test if a single channel approach can be used to derive the land surface temperature globally. For this reason we test a simple linear relation that is derived from the ground observations (Table 1) and the AMSR-E 37 Ghz, vertical polarized channel. Three sites are excluded from this analysis because the flux tower is not representative for the satellite footprint. The excluded sites are sites F, Cabauw, Netherlands, too much open water; Q, Yatir, Israel, small forest in barren surroundings; and H, Mitra2, Portugal, a grass site in open Oak woodland. The resulting sites have a range of different vegetation types and climates. Figure 4 shows the scatter plot of all the data. The relationship between $T_{B,37V}$ and T_s that best describes these observations is:

$$T_s = 1.11T_{B,37V} - 15.2 \qquad for\ T_{B,37V} > 259.8 \qquad (2)$$

[29] The corresponding error of 4.5 K and correlation of $R^2 = 0.84$ are the upper limit of expected error for this method and reflect errors in the model, in the ground measurement and errors due to the heterogeneity of the satellite footprint as compared to the ground site. The lower threshold of suitable brightness temperatures of 259.8 K marks the divide between frozen and unfrozen conditions at a physical temperature of 273.15 K. The change in emission is highly nonlinear over this phase change, and is not covered by the regression equation. The errors as caused by this simplification of the radiative transfer model are evaluated in simulation experiments in the following two sections. In section 3.4, the ground sites will be analyzed individually to assess the errors resulting from the ground measurements and heterogeneity of the satellite footprint.

3.2. Error Simulations

[30] The simplification of the radiative transfer model into a single linear relationship (equation (2)) causes a difference in the retrieved T_s if the actual parameters deviate from the default scenarios. Assuming that the T_s as derived from the radiative transfer model is the "true" temperature, the deviation from this value is regarded as an error. The potential size of these errors is estimated for each input parameter individually. In Figures 5–7 the most important parameters are tested for their influence on the deviation in T_s as compared to the linear relation. In Figures 5–7 the calibrated value of the evaluated parameter is indicated by a vertical dotted line.

[31] Figure 5a shows how T_s will be affected by soil moisture at different vegetation densities. For a surface with dense vegetation ($\Gamma_v = 0.2$), the error as introduced by the soil moisture conditions will not exceed 1.5 K. However, the soil moisture content becomes critical for a vegetation transmissivity greater than 0.35. As the vegetation density decreases, the range of W_c values that result in a bias within the acceptable limits decreases. At the same time, the W_c that minimizes the bias, decreases from the default value of 25% at $\Gamma_v = 0.2$, to 21% for $\Gamma_v = 0.35$, to 15% for a sparsely vegetated surface with $\Gamma_v = 0.5$. Although the error in the retrieved T_s over areas with low vegetation densities can be within the limits for part of the year, it is likely that it exceeds the limit for some parts of the year. For this reason applying the T_s retrieval to areas where the Γ_v is higher than 0.5 should be done with caution because small variations in W_c will result in a high bias. These areas roughly correspond to IGBP classes barren and sparsely vegetated and open shrublands.

[32] Also shown in Figure 5 are the effect on T_s of the single scattering albedo, roughness, and wilting point at $\Gamma_v = 0.2$ and $\Gamma_v = 0.5$. The errors for the intermediate

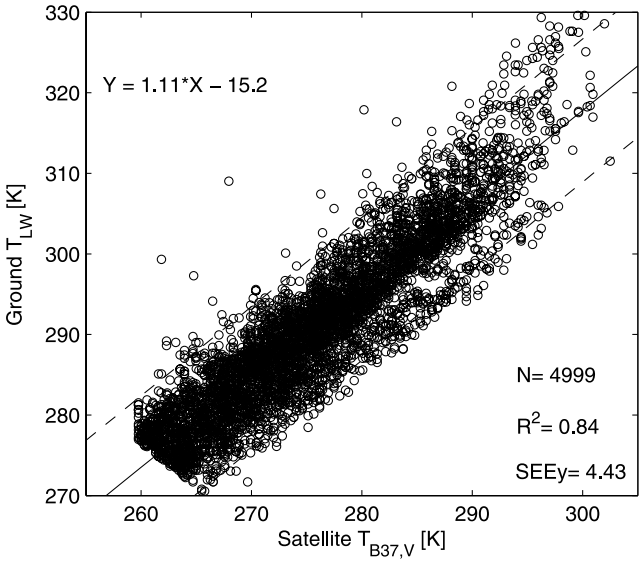

Figure 4. Regression of satellite observations against ground observations of 14 FLUXNET sites.

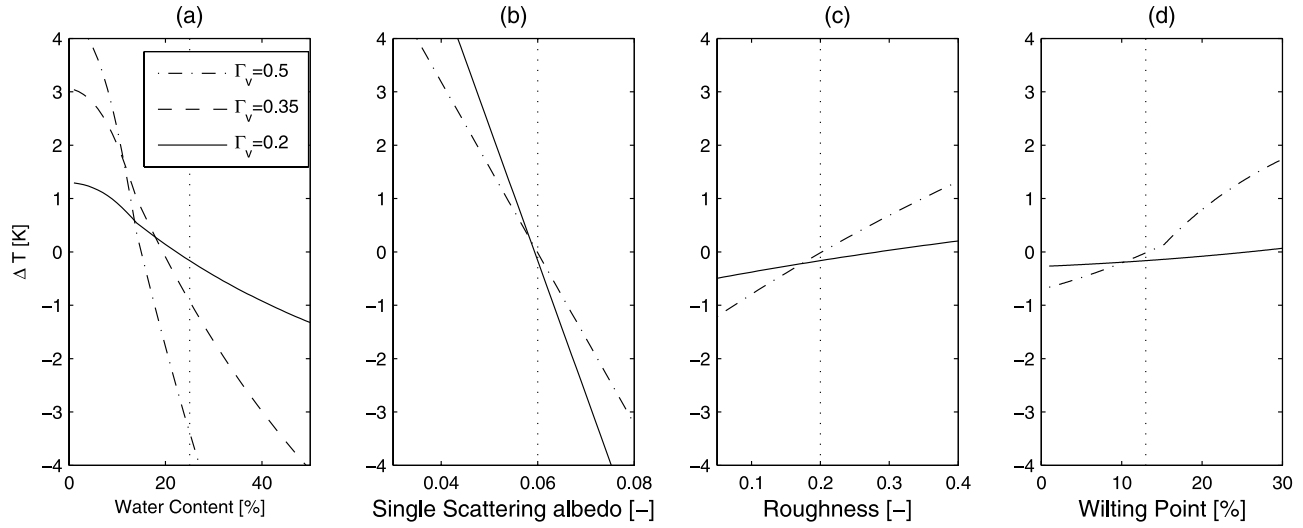

Figure 5. Deviations in T_s (ΔT (K)) from vegetated configuration for selected parameters. Vertical line indicates calibrated value.

vegetation value ($\Gamma_v = 0.35$) are not shown for these plots, but are understood to be in between the given examples. The corresponding moisture value is chosen that minimizes the error, respectively 25% and 15% (see Figure 5a). The single scattering albedo (Figure 5b) has a strong effect on the error when the vegetation is dense. The roughness (Figure 5c) has a much smaller effect and is not expected to result in errors of more than 1 K for vegetation densities with $\Gamma_v < 0.5$. The texture, and in particular the wilting point, results in errors similar to the roughness, although less linear (Figure 5d). It does not affect the $T_{B,37V}$ in the most densely vegetated scenario, but for surfaces with less dense vegetation the error can increase to 2 K for a silt loam at $\Gamma_v = 0.5$.

[33] The same parameters are tested for a dry, bare surface (see Table 2). The effect of soil moisture under these conditions is extremely strong (see Figure 6a, and note that the axis in Figure 6a is elongated). The moisture value with minimal error is now only 8% and the moisture range with acceptable errors is very small. The single scattering albedo (Figure 6b) has now a weak effect on the error because the vegetation is very sparse. The roughness (Figure 6c) and texture (Figure 6d) have a strong effect in this scenario but are not expected to result in errors of more than 3 K. The wilting point in particular will in general be low for desert type scenarios.

[34] Not all satellite radiometers have exactly the same frequency channel and incidence angle within the Ka band (see Figure 1). In the simulations an incidence angle of 55° is used, but historically incidence angles between 50° and 55° have been used. For vegetated surfaces this is not expected to make a significant impact, but for bare surfaces this results in a maximum bias of −1 K at 50° (Figure 7a). The exact frequency of the Ka band channel for most radiometers has been 37.0 GHz, only for the latest AMSR-E instrument this channel is at 36.5 GHz. This small difference is not expected to affect the results (Figure 7b), but it can cause small differences in the atmospheric transmissivity.

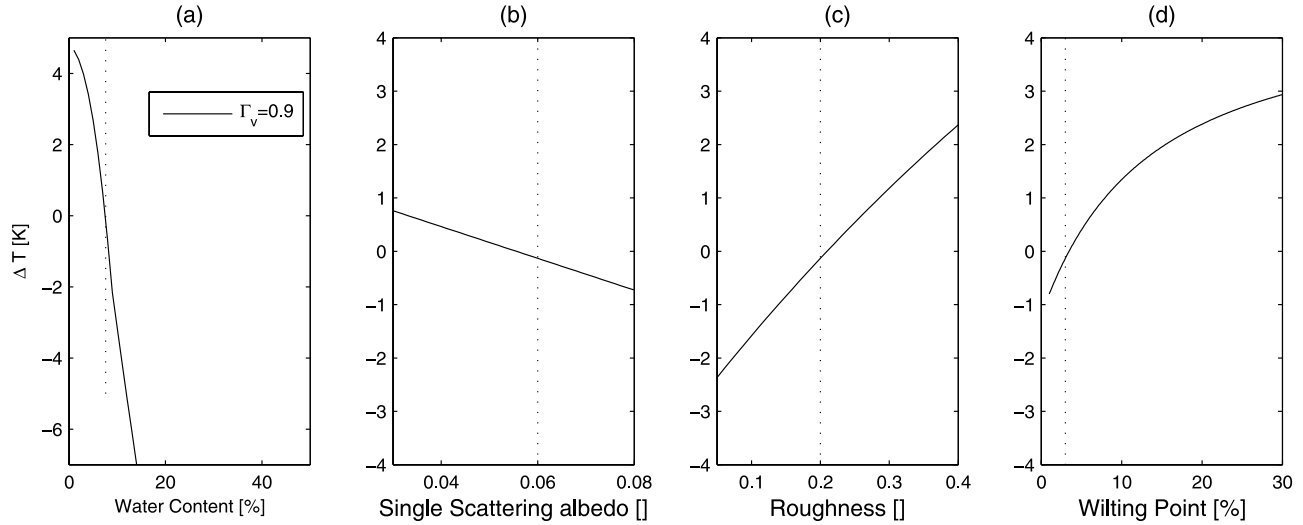

Figure 6. As Figure 5, for bare configuration.

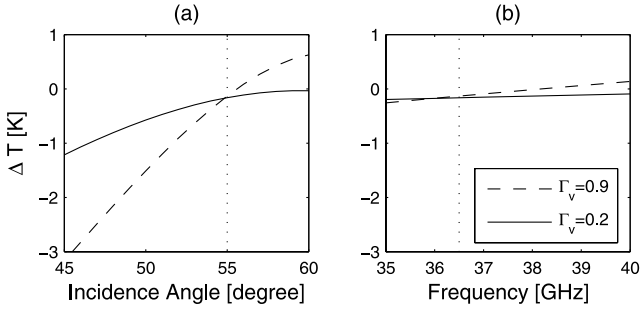

Figure 7. As Figure 5, for frequency and incidence angle.

[35] Finally, open water will cause a negative bias in the retrieved temperature because the emissivity for water surfaces is much lower then for land. Assuming that the water has the same temperature as the land surface, the bias can be estimated by calculating both open water and land surface brightness temperatures. Such analysis shows that for a vegetated land surface the bias as a function of the fraction of open water (F) is: ($\Delta T = -0.72F$). This means that the bias will exceed 3 K if the fraction of open water in the satellite footprint exceeds 4%. Therefore 4% should be the maximum accepted fraction of open water when applying this method, but preferably lower if a higher accuracy is required.

[36] The conclusion of these simulations can be summarized as follows. For vegetated surfaces, the effect of soil parameters is muted if the vegetation is dense ($\Gamma_v \leq 0.2$). The effect of soil moisture becomes important for less dense vegetation, with errors of ±3 K at $\Gamma_v = 0.35$. The vegetation parameter single scattering albedo has the most effect on the error, and is calibrated at $\omega = 0.06$. This parameter is subsequently used as a global constant. At dry, almost bare surfaces, the effect of soil parameters is very strong and that of vegetation parameters is of course very small. Soil moisture has an extreme effect in this scenario. The roughness parameter h and Q have a strong effect on the error too, and are calibrated at $h = 0.2$ and $Q = 0.2$. These parameters are subsequently considered to be constant over time, and over the globe.

3.3. Global Error Simulation

[37] In actual applications of equation (2) on global Ka band observations, some of the above mentioned error sources will cancel each other out. For example, vegetation density and soil water content are, generally speaking, positively related. As was shown, the soil moisture values that minimize the error are also positively related with vegetation density. This section explores the bias associated with the use of equation (2) as opposed to the radiative transfer model, and as a result of the main spatially varying parameters. For this purpose, the radiative transfer model is applied to observed global input parameters and the resulting modeled brightness temperatures are compared with equation (2). Observed brightness temperatures are acquired from AQUA AMSR-E for 1 and 2 July 2004, for the ascending path with an equator crossing time of ~1330 local time. In the radiative transfer model as described in section 2.4 all error sources are either not related, or positively related with temperature. It follows that these midday values will give a high estimate of the expected bias, especially for the Northern Hemisphere, where it is summer.

[38] First, T_s is calculated from the observed $T_{B,37V}$ according to equation (2) (Figure 8c). Temperatures below freezing are removed, as are grid cells with more than 4% open water. Secondly, soil moisture data are used as derived from $T_{B,10}$ with the Land Parameter Retrieval Model (LPRM) [*Owe et al.*, 2008]. The LPRM soil moisture retrieval does not yield moisture values when the vegetation is too dense. These areas are masked in Figure 8b, and are assigned a soil moisture of $W_c = 25\%$ in the simulation. This arbitrary value does not affect the following discussion because the dense vegetation effectively blocks the emission from the soil. Third, the atmospheric transmissivity is parameterized according to *Choudhury et al.* [1992] using precipitable water and cloud optical thickness data from the International Satellite Cloud Climatology Project (ISCCP [*Rossow and Schiffer* 1991]). The effective air temperature is calculated as a direct function of surface temperature [*Bevis et al.*, 1992]. Because of this simplification, possible errors due to asynchronous variations in the difference between surface and air temperature are avoided. Finally, the vegetation transmissivity (Figure 8a) is parameterized by means of the Microwave Polarization Difference Index (MPDI) according to *Meesters et al.* [2005]. The MPDI is calculated from the Ka band brightness temperatures:

$$MPDI = \frac{T_{B,V} - T_{B,H}}{T_{B,V} + T_{B,H}} \tag{3}$$

The atmospheric effect on this MPDI value is removed to obtain the top of vegetation MPDI.

[39] These global maps of input data are subsequently used to simulate the $T_{B,37V}$ according to the radiative transfer theory (see section 2.4). The difference between simulated and measured $T_{B,37V}$ is the error as introduced by the simplification of the radiative transfer model to a single linear relationship (equation (2)). The error in brightness temperature is subsequently multiplied by the slope of the linear relationship to yield the corresponding error in T_s.

[40] Figure 8d shows the global distribution of the bias in the retrieved T_s, due to spatial variation in soil moisture, soil texture, vegetation density and atmospheric vapor content. It can be seen that for large parts of the world this spatial variation in soil vegetation and atmospheric variables will not result in large errors in T_s. This is because, for 53% of the globe, the transmissivity is less than 0.35 and for 72% the Γ_v is less than 0.5. As was discussed above, areas where $\Gamma_v > 0.5$ are expected to have a bias exceeding 3 K for at least part of the year. Areas with low vegetation and saturated soil moisture conditions show a high negative bias (see for example Canada). This negative bias is increased if there is some open water in the pixel. Overall, for the land area with $\Gamma_v < 0.5$, 94% has a bias less than 3 K. This fraction decreases to 87% for a bias of <2 K, and 69% for a bias <1 K.

[41] The relationship between the land surface temperature bias and the vegetation transmissivity is illustrated in Figure 9 for the entire range of vegetation densities. Horizontal lines indicate the 3 K limits, with 83% of the data (including the desert areas) within these limits. The data are also divided into three groups based on soil moisture

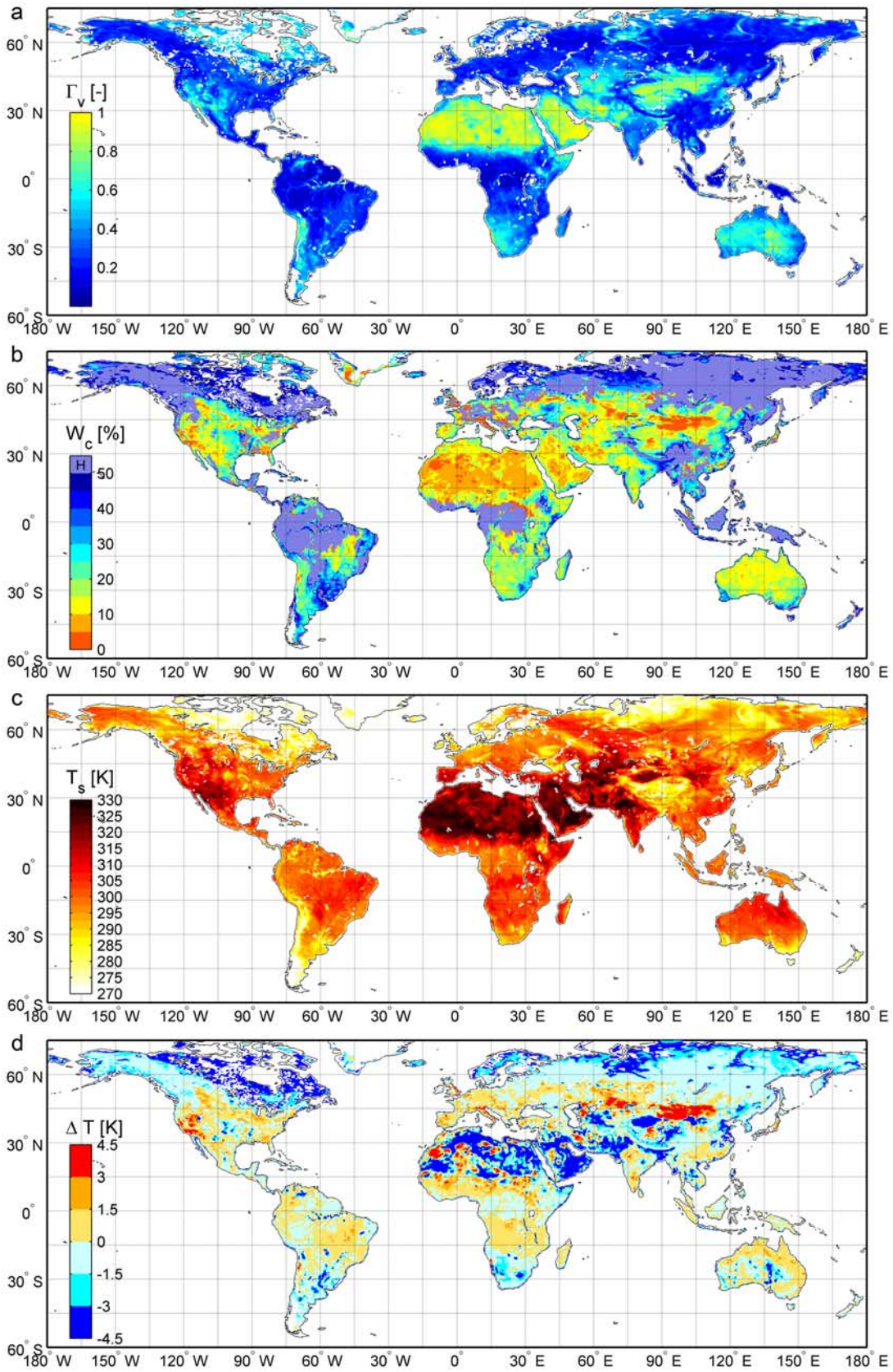

Figure 8. Main input and results of global error simulation. (a) Vegetation transmissivity at 37 GHz, (b) soil moisture from LPRM-X with high vegetation densities masked (H), (c) land surface temperature (K), and (d) bias (uation (2), radiative transfer model)). The data are averaged for 1 and 2 July 2004.

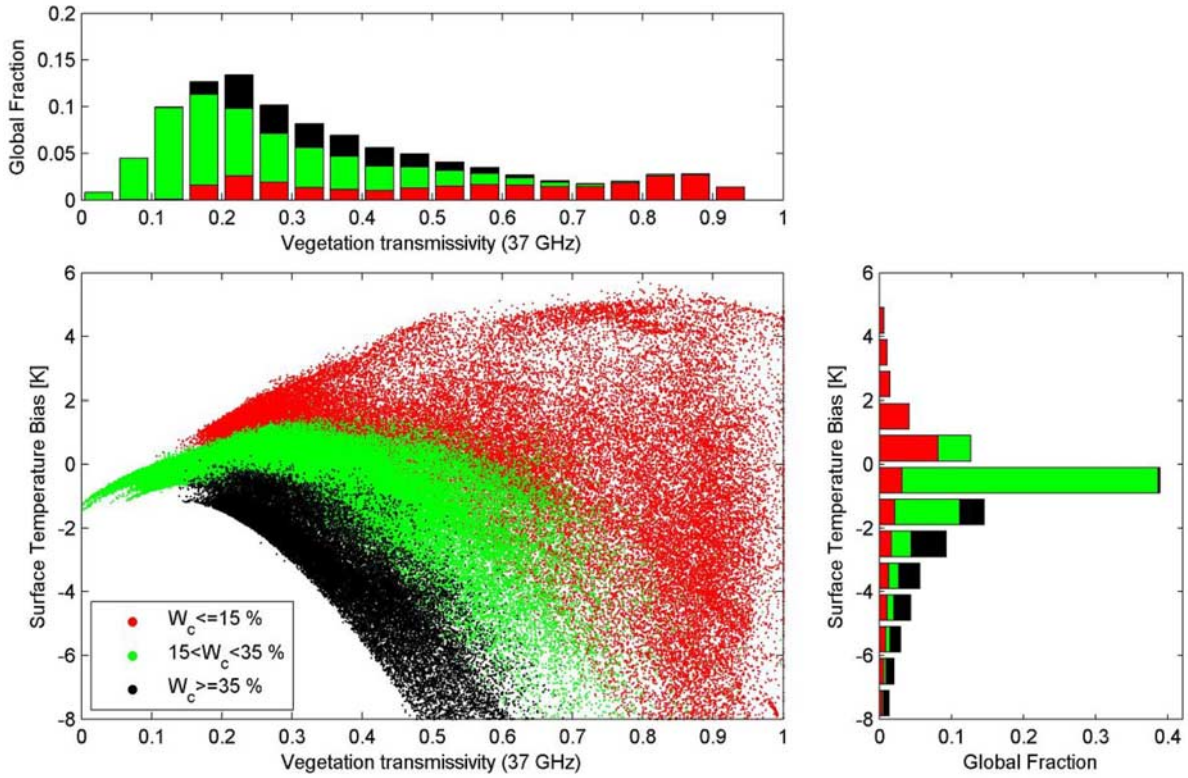

Figure 9. Scatter diagram of the vegetation transmissivity against the bias (ΔT (K)), together with the associated histograms for both variables. In red are the values with $W_c < 15\%$, in black are values with $W_c > 35\%$, and green are intermediate moisture values.

content. The vertical line indicates the vegetation transmissivity at which soil moisture becomes a critical factor in the accuracy of the relationship for a 3 K limit. From Figure 9 it can also be seen that for the pixels with low vegetation density ($\Gamma_v > 0.5$) a large number of pixels is still within acceptable limits. In these situations, the negative bias associated with the low vegetation density is offset by a positive bias, for example due to a very low soil moisture content. However, these same pixels are likely to fall outside the limits for some of the year if the moisture conditions change.

[42] In the above, the parameters for roughness (h, Q), and the single scattering albedo are treated as global constants. Errors due to possible variations in these parameters are evaluated in the Monte Carlo simulation for the same data as described above. Global fields of roughness (h, Q) and single scattering albedo are not available and are attributed random deviations from a given mean. The estimated standard deviation associated with these parameters is listed in Table 2. In the Monte Carlo simulation this is repeated 500 times, so that the average of the deviations again approximates the standard deviation for each parameter. Figure 10 shows the result of 500 iterations of the Monte Carlo simulation. The histograms show the distribution of the input parameters. The standard error of the resulting temperature relationship is 1.9 K. The average regression is indicated by the solid black line, and the standard error bounds by the dashed lines.

[43] The conclusion from these global simulations is that for large parts of the E e surface conditions are such that the error associated with equation (2) is within acceptable limits. Areas with unfavorable conditions have either (1) practically no vegetation or (2) sparse vegetation and almost saturated soil moisture conditions.

3.4. Ground Validation

[44] Equation (2) is validated by comparing temperature retrievals with ground observations of T_{LW} from the FLUXNET stations described earlier. The procedure for deriving T_{LW} is outlined in section 2.2. Since equation (2) is based on data from most of these sites in the first place, we cannot validate the absolute accuracy of this method. However, it is possible to determine the precision of this method by looking at the standard error for each site individually.

[45] The comparisons of the satellite derived T_s and T_{LW} derived for the field site are shown in Figure 11 and summarized in Figure 12. The field sites are separated into a group with low vegetation and one with high vegetation. The low-vegetation group consists of the grassland, open shrubland and cropland sites. The high-vegetation group includes all the forest sites (see Table 1). For both groups, correlations are high, with a median of $R^2 = 0.9$ for the low-vegetation group and $R^2 = 0.93$ for the high-vegetation group. The standard error of estimate (SEE) shows a clear differentiation between the two groups. For forests, the SEE is between 1.5 and 2.5 K, with a median of 2.2 K. The low vegetation has SEE values between 2.3 and 4.5 K, with a median of 3.5 K. A factor that might explain some of the difference in performance between the low- and high-vegetation sites, is the seasonality in the longwave emissivity

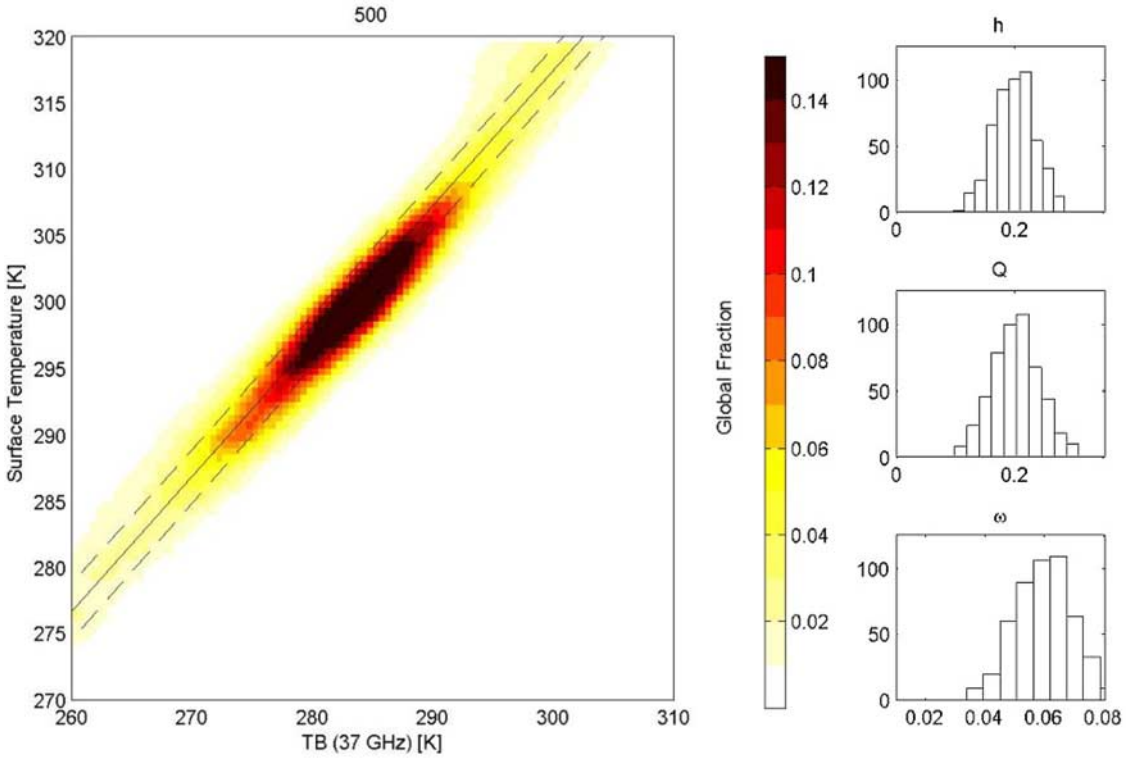

Figure 10. Simulated $T_{B,37V}$ according to equation (2) for the globe.

as observed in the low-vegetation sites (see Figure 3). The emissivity through the year at these sites is affected by the growing season of the vegetation. For this analysis, a constant ε is used for the entire year. On the whole, these results indicate that T_s can be derived with a precision of 3.5 K for low vegetation and 2.2 K for forests.

[46] Because of the inherent difficulties of comparing satellite data representing footprints of 25 × 25 km to single point observations, it is difficult to use this analysis to further constrain the accuracy as determined from the simulations. This is because the temperature at the ground site is not necessarily a good representation for the satellite footprint. If the vegetation density at the ground site is low, but the satellite footprint contains some forest, the temperature cycles (diurnal and seasonal) will likely be more pronounced at the field site. As a result, the slope of the regression will be above unity (e.g., site A). The opposite will happen if the ground site is located in a forest and the satellite footprint also contains less dense vegetation. This can result in a corresponding slope of below unity (e.g., site Q). The box plot of the slope of the regression lines shows that both these effects happen within the selected field sites (see Figure 12). The slope for the low-vegetation sites is between 1 and 1.37, and for the high vegetation between 0.74 and 1.04. This means a large part of the variation in the slopes of the observed regression lines can be explained by heterogeneity in the satellite footprint and does not reflect an error in the satellite temperature. Another example of a point-to-pixel effect happens when there is a high amount of open water in the satellite footprint. This causes a large negative bias in the satellite derived temperature, and as a result the offset of the regression is too high (e.g., site F). This effect does reflect an error in the satellite temperature and should be avoided by applying a strict mask for open water.

[47] With this simple method to obtain T_s from $T_{B,37V}$ it is possible to observe the diurnal temperature variation, using multiple satellites. This is shown in Figure 13 for the first 2 weeks of June 2006, for the forest site in North Carolina, USA (site P). The satellites describe the diurnal cycle of the ground measurements very well. Only at one instance, on 7 June, precipitation causes a serious negative error. After removing the observations that occur during rainfall, the RMS error between satellite and ground observations is 1.4 K, with a correlation of $R^2 = 0.94$. Figure 14 shows a second example for 2 weeks of June 2006, this time for the grassland site in Montana, USA (site B). Again at one instance, on 6 June, precipitation causes a negative error. Although the analysis of the full year of data showed this site performing worse than the North Carolina site, this 2 week period still shows a reasonably good RMS error between satellite and ground observations of 2.1 K, and a correlation of $R^2 = 0.90$.

4. Discussion and Conclusion

[48] The Ka band vertical polarized passive microwave channel has a strong and linear relationship with the physical land surface temperature. It is shown that with a simple linear relationship the T_s can be obtained for nonfrozen land surfaces and areas with little or no open water (<4%). The bias of the T_s is estimated to be within 1 K for 60% of the remaining land surface. This fraction increases to 69% if areas with sparse vegetation or bare soil are excluded. The method requires no correction factors, and fully preserves the

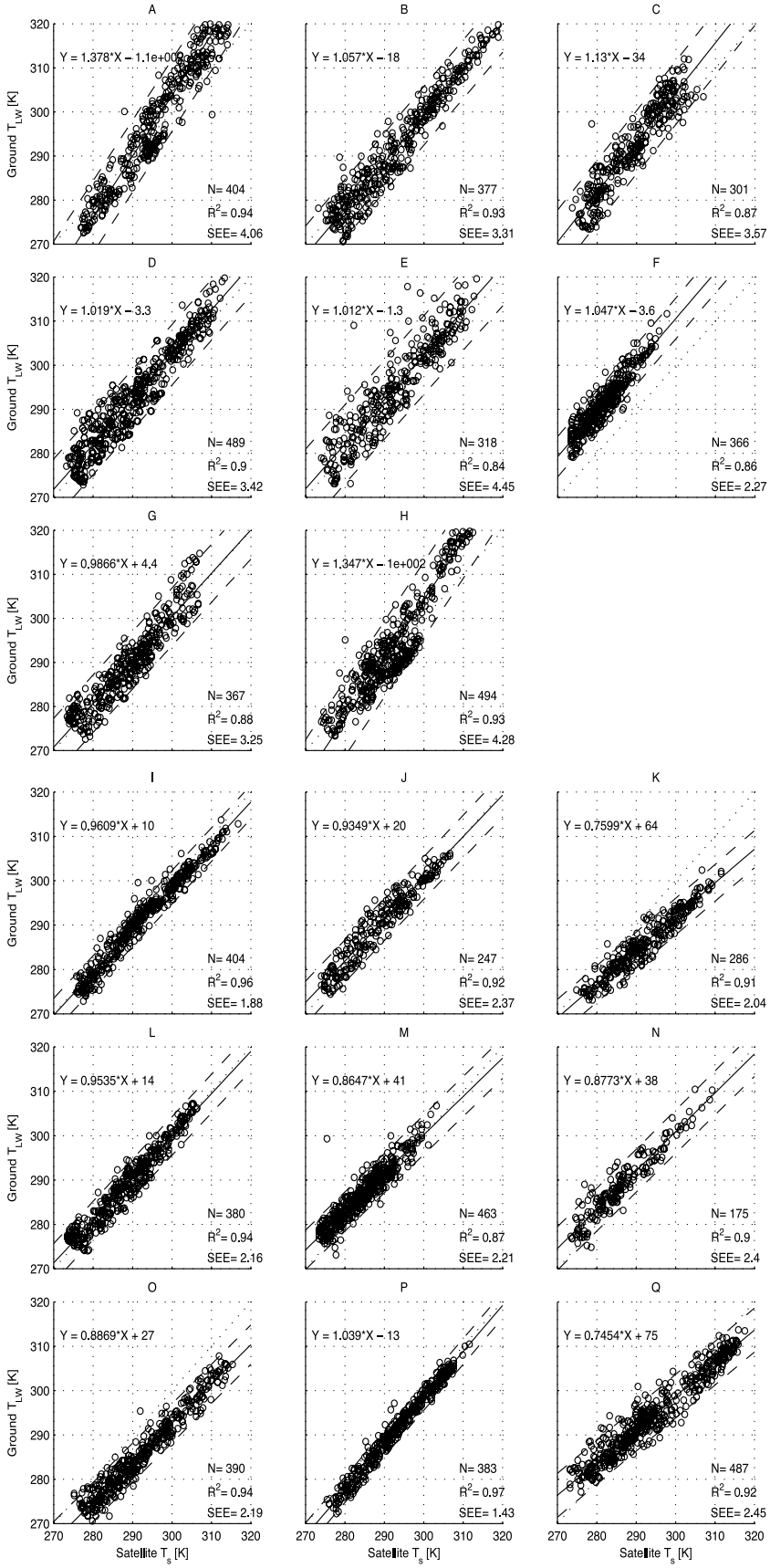

Figure 11. Satellite derived T_s is compared to ground measurements of T_{LW} for 17 locations during 2005. The letters above each plot refer to the site IDs in Table 1.

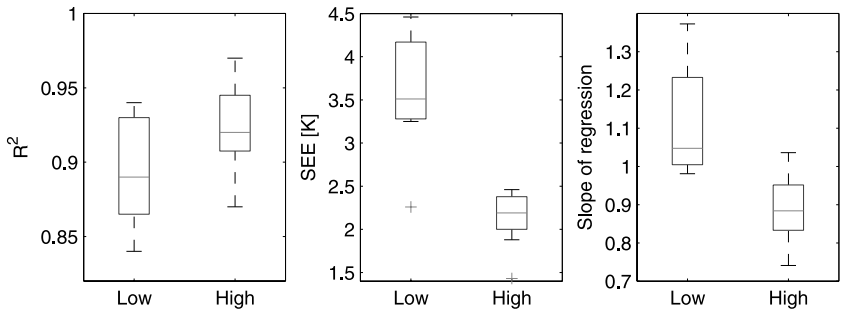

Figure 12. Satellite derived T_s is compared to ground measurements of T_{LW} for 17 locations during 2005. The box plots have horizontal lines between each data quartile of the selections for low vegetation (low) and high vegetation (high). Outliers are indicated with pluses.

original observed signal. The satellite observed T_s represents the area weighted average of the different land covers in the sensors view and can therefore best be compared to the longwave temperature and not with a soil or vegetation temperature at a fixed depth. A comparison of the retrieved temperature with ground observations of longwave temperature yielded a SEE of ~3.5 K for low vegetation and ~2.5 for forest, individually for each site. These errors result from (1) the precision of the microwave sensor (0.6 K for AMSR-E), (2) a temporal change in the bias as introduced by the model and nonstatic surface characteristics, (3) a temporal change in heterogeneity effects of the site versus the pixel, and (4) precision and accuracy of the longwave measurements. The last two points are purely caused by the validation method, and do not reflect an actual error with the area averaged temperature. For this reason, the SEE values are expected to represent an upper limit for the precision of the retrieved land surface temperature. If this method is applied to all available vertically polarized 37 GHz observations, a 30 year record of land surface temperature can be obtained. For much of this period this set would include several observations per day. Complicating the interpretation of such a long-term data set would be the different overpass times for each satellite and possibly orbital decay over a satellites lifetime.

[49] For periods with multiple observations per day it is shown that the diurnal temperature cycle can be approximated from remote sensing data with a surprisingly high precision. Because the partitioning of the surface energy balance is strongly related to surface temperature, the amplitude of the diurnal temperature variation can be of value for studies of latent and sensible heat fluxes at a global scale. Since such studies make use of temperature differences, the possible bias in the observations is less of a problem.

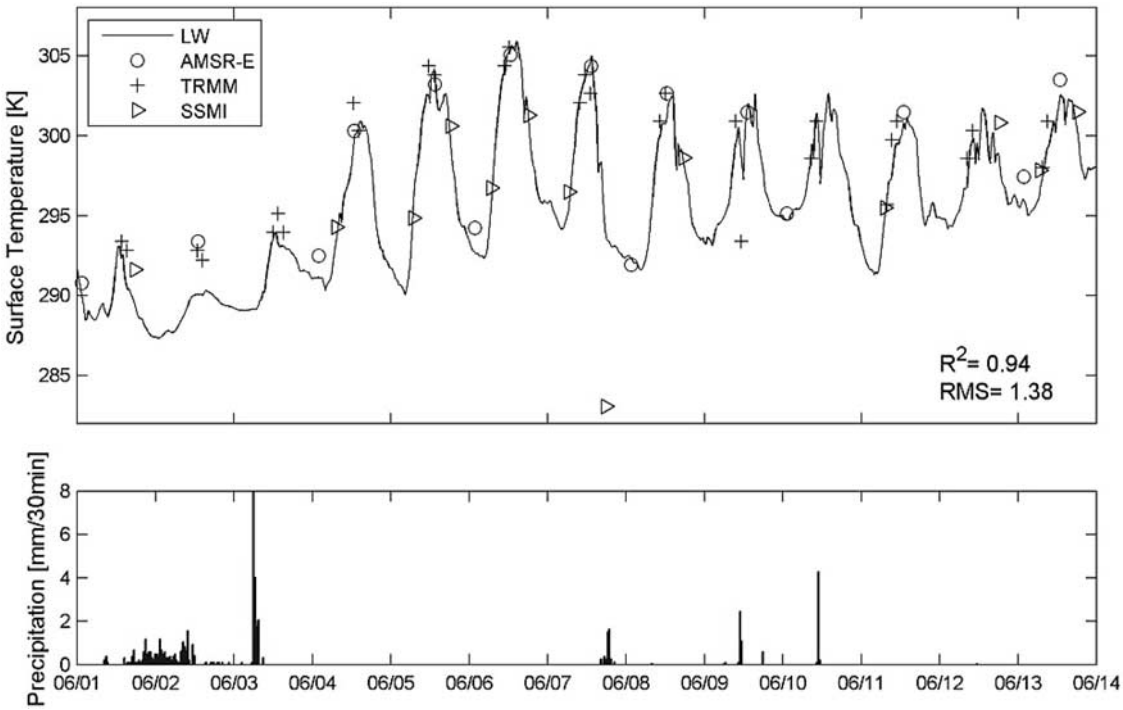

Figure 13. Diurnal temperature cycles as measured at a field site in North Carolina, USA, and observed by satellites.

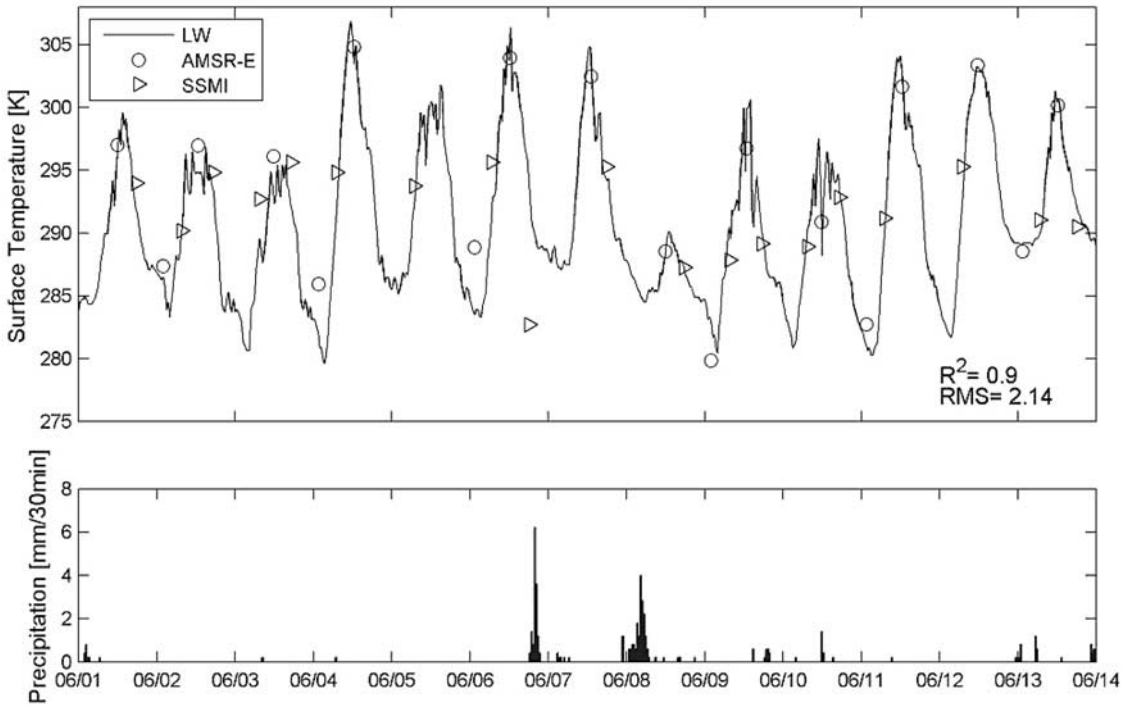

Figure 14. Diurnal temperature cycles as measured at a field site in Montana, USA, and observed by satellites.

However, further research will be necessary to widen the scope of this approach in sparsely vegetated areas.

[50] **Acknowledgments.** This work was partly funded by the EU 6th Framework program WATCH (project 036946-2). We appreciate the help from Michiel van der Molen with the longwave emissivity derivation and the helpful comments of John Gash. We thank the organizations who support the FLUXNET sites (Illinois State Water Survey, INRA, Max Planck Institute Jena, NOAA/ARL, Universidade Técnica de Lisboa, University of Tuscia Viterbo, Wageningen University, and Weisman Institute of Science) for making the data available to us.

References

Anthoni, P. M., A. Knohl, C. Rebmann, A. Freibauer, M. Mund, W. Ziegler, O. Kolle, and E. Schulze (2004), Forest and agricultural land-use-dependent CO_2 exchange in Thuringia, Germany, *Global Change Biol.*, *10*(12), 2005–2019.

Armstrong, R., K. Knowles, M. Brodzik, and M. Hardman (1994), DMSP SSM/I pathfinder daily EASEGrid brightness temperatures, http://www.nsidc.org/data/nsidc-0032.html, Natl. Snow and Ice Data Cent., Boulder, Colo.

Ashcroft, P., and F. Wentz (2003), AMSR-E/AQUA L2A global swath spatially-resampled brightness temperatures (Tb) v001, http://www.nsidc.org/data/ae_l2a.html, Natl. Snow and Ice Data Cent., Boulder, Colo., (Updated daily.)

Baldocchi, D., et al. (2001), FLUXNET: A new tool to study the temporal and spatial variability of ecosystem-scale carbon dioxide, water vapor, and energy flux densities, *Bull. Am. Meteorol. Soc.*, *82*, 2415–2434.

Beljaars, A., and F. Bosveld (1997), Cabauw data for the validation of land surface parameterization schemes, *J. Clim.*, *10*(6), 1172–1193.

Belward, A. S., J. E. Estes, and K. D. Kline (1999), The IGBP-DIS global 1-km land-cover data set DISCover: A project overview, *Photogramm. Eng. Remote Sens.*, *65*, 1013–1020.

Bevis, M., S. Businger, T. Herring, C. Rocken, R. Anthes, and R. Ware (1992), GPS meteorology—Remote-sensing of atmospheric water-vapor using the global positioning system, *J. Geophys. Res.*, *97*, 15,787–15,801.

Calvet, J., J. Wigneron, A. Chanzy, S. Raju, and L. Laguerre (1995), Microwave dielectric properties of a silt-loam at high frequencies, *IEEE Trans. Geosci. Remote Sens.*, *33*, 634–642.

Choudhury, B. J., E. R. Major, E. Smith, and F. Becker (1992), Atmospheric effects on SMMR and SSM/I 37 GHz polarization difference over the Sahel, *Int. J. Remote Sens.*, 3443–3463.

Colwell, R., D. Simonett, and F. Ulaby (Eds.) (1983), *Manual of Remote Sensing*, vol. 2, *Interpretation and Applications*, 2nd ed., Am. Soc. of Photogramm., Falls Church, Va.

David, T. S., M. I. Ferreira, S. Cohen, J. Pereira, and J. David (2004), Constraints on transpiration from an evergreen oak tree in southern Portugal, *Agric. For. Meteorol.*, *122*, 193–205.

DeAngelis, R., P. Valentini, G. Matteucci, R. Monaco, S. Dore, and G. E. S. Mugnozza (1996), Seasonal net carbon dioxide exchange of a beech forest with the atmosphere, *Global Change Biol.*, *2*(3), 199–207.

De Jeu, R. A. M., and M. Owe (2003), Further validation of a new methodology for surface moisture and vegetation optical depth retrieval, *Int. J. Remote Sens.*, *24*(22), 4559–4578.

Dolman, A., E. Moors, and J. Elbers (2002), The carbon uptake of a mid latitude pine forest growing on sandy soil, *Agric. For. Meteorol.*, *111*(3), 157–170.

Fily, M., A. Royer, K. Goïta, and C. Prigent (2003), A simple retrieval method for land surface temperature and fraction of water surface determination from satellite microwave brightness temperatures in sub-arctic areas, *Remote Sens. Environ.*, *85*, 328–338.

Grunzweig, J. M., T. Lin, E. Rotenberg, A. Schwartz, and D. Yakir (2003), Carbon sequestration in arid-land forest, *Global Change Biol.*, *9*(5), 791–799.

Hollinger, S., C. Bernacchi, and T. Meyers (2005), Carbon budget of mature no-till ecosystem in north central region of the united states, *Agric. For. Meteorol.*, *130*, 59–69.

Kerr, Y. H., P. Waldteufel, J.-P. Wigneron, J.-M. Martinuzzi, J. Font, and M. Berger (2001), Soil moisture retrieval from space: The Soil Moisture and Ocean Salinity (SMOS) mission, *IEEE Trans. Geosci. Remote Sens.*, *39*(8), 1729–1735.

Kowalski, S., M. Sartore, R. Burlett, P. Berbigier, and D. Loustau (2003), The annual carbon budget of a French pine forest (pinus pinaster) following harvest, *Global Change Biol.*, *9*(7), 1051–1065.

Kummerow, C., W. Barnes, T. Kozu, J. Shiue, and J. Simpson (1998), The Tropical Rainfall Measuring Mission (TRMM) sensor package, *J. Atmos. Oceanic Technol.*, *15*, 809–817.

Meesters, A. G. C. A., R. A. M. De Jeu, and M. Owe (2005), Analytical derivation of the vegetation optical depth from the Microwave Polarization Difference Index, *IEEE Geosci. Remote Sens. Lett.*, *2*(2), 121–123, doi:10.1109/LGRS.2005.843983.

Mo, T., B. J. Choudhury, and T. Jackson (1982), A model for microwave emission from vegetation-covered fields, *J. Hydrol.*, *184*, 101–129.

Njoku, E., T. Jackson, V. Lakshmi, T. Chan, and S. Nghiem (2003), Soil moisture retrieval from AMSR-E, *IEEE Trans. Geosci. Remote Sens.*, *41*, 215–229.

Owe, M., and A. Van de Griend (2001), On the relationship between thermodynamic surface temperature and high-frequency (37 GHz) vertically polarized brightness temperature under semiarid conditions, *Int. J. Remote Sens.*, *22*, 3521–3532.

Owe, M., R. A. M. De Jeu, and J. P. Walker (2001), A methodology for surface soil moisture and vegetation optical depth retrieval using the microwave polarization difference index, *IEEE Trans. Geosci. Remote Sens.*, *39*(8), 1643–1654.

Owe, M., R. De Jeu, and T. Holmes (2008), Multi-sensor historical climatology of satellite derived global land surface moisture, *J. Geophys. Res.*, *113*, F01002, doi:10.1029/2007JF000769.

Pampaloni, P., and S. Paloscia (1986), Microwave emission and plant water content: A comparison between field measurements and theory, *IEEE Trans. Geosci. Remote Sens.*, *24*, 900–905.

Penman, H. L. (1948), Natural evaporation from open water, bare soil and grass, *Proc. R. Soc. London, Ser. A*, *193*, 120–145.

Rossow, W., and R. Schiffer (1991), ISCCP cloud data products, *Bull. Am. Meteorol. Soc.*, *71*, 2–20.

Rossow, W., A. Walker, and L. Gardner (1993), Comparison of ISCCP and other cloud amounts, *J. Clim.*, *6*, 2396–2416.

Scherer-Lorenzen, M., E. Schulze, A. Don, J. Schumacher, and E. Weller (2007), Exploring the functional significance of forest diversity: A new long-term experiment with temperate tree species (BIOTREE), *Perspect. Plant Ecol. Evol. Syst.*, *9*, 53–70, doi:10.1016/j.ppees/2007.08.002.

Snyder, W. (1999), Classification-based emissivity for land surface temperature measurement from space, *Int. J. Remote Sens.*, *19*, 2753–2774.

Ulaby, F. T., R. K. Moore, and A. K. Fung (1986), *Microwave Remote Sensing: Active and Passive*, vol. III, *From Theory to Applications*, Artech House, Norwood, Mass.

Van de Griend, A. A., and M. Owe (1994), Microwave vegetation optical depth and signal scattering albedo from large scale soil moisture and NIMBUS/SMMR satellite observatons, *Meteorol. Atmos. Phys.*, *54*, 225–239.

Verstraeten, W., F. Veroustraete, C. Van der Sande, I. Grootaers, and J. Feyen (2006), Soil moisture retrieval using thermal inertia, determined with visible and thermal spaceborne data, validated for European forests, *Remote Sens. Environt.*, *101*, 299–314.

Wang, J. R., and B. J. Choudhury (1981), Remote sensing of soil moisture content over bare field at 1.4 GHz frequency, *J. Geophys. Res.*, *86*(C6), 5277–5287.

Wang, J. R., and T. J. Schmugge (1980), An empirical model for the complex dielectric permittivity of soils as a function of water content, *IEEE Trans. Geosci. Remote Sens.*, *18*(4), 288–295.

R. A. M. De Jeu, A. J. Dolman, and T. R. H. Holmes, Department of Hydrology and Geo-Environmental Sciences, Vrije Universiteit, NL-1081 HV Amsterdam, Netherlands. (thomas.holmes@falw.vu.nl)

M. Owe, Hydrological Sciences Branch, NASA Goddard Space Flight Center, Greenbelt, MD 20771, USA.